AIAA JOURNAL
Vol. 42, No. 3, March 2004

Experimental and Numerical Characterization of the Mechanical Behavior of Aeronautical Aluminum Alloys

Diego J. Celentano,* Alberto E. Monsalve,† and Alfredo Artigas†
Universidad de Santiago de Chile, Santiago, Chile

An experimental and numerical study is presented of the mechanical behavior during the conventional tensile test of three different aluminum alloys extensively used in aeronautical applications: 7075 T7351, 7050 T7451, and 2024 T3. A set of experiments has been carried out with cylindrical specimens in order to obtain the elastic and hardening parameters that characterize the material response. Moreover, a finite element large-strain elastoplasticity-based formulation is proposed and used to simulate the deformation process during the whole test. Finally, the results obtained with the simulation are experimentally validated.

I. Introduction

THE tensile test is an important standard engineering procedure useful to characterize some relevant elastic and plastic variables related to the mechanical behaviour of materials. Because of the nonuniform stress and strain distributions existing at the neck for high levels of axial deformation, it has been long recognized that significant changes in the geometric configuration of the specimen have to be considered in order to properly describe the material response during the whole deformation process up to the fracture stage.

Although in many engineering applications the design of structural parts is restricted to the elastic response of the materials involved, the knowledge of their behaviors beyond the elastic limit is relevant because plastic effects with usually large deformations take place in the previous manufacturing procedures such as forming, forging, etc.

The necking process of a bar used in the tensile test has been extensively studied by means of analytical expressions for the stress distribution at the neck based on some geometric considerations of the deformation pattern (for example, see Refs. 1 and 2). In recent years, several finite element large-strain formulations usually defined within the plasticity framework have been developed and applied to the analysis of this test under isothermal and nonisothermal conditions (for example, see Refs. 3–8 and references therein). Moreover, some of such formulations have been validated, generally under isothermal conditions, with experimental data considering different materials.

The aim of this paper is to present an experimental analysis and a numerical simulation of the mechanical behavior during the tensile test experienced by cylindrical specimens of three widely used aeronautical aluminum alloys: 7075 T7351, 7050 T7451, and 2024 T3. As it is well known, the first two alloys have been mainly designed for structural parts (e.g., beams) whereas the third one is mostly utilized in fuselages (with a typical thickness of 2 mm approximately), rudders, and elevators. The experimental procedure undertaken to characterize some specific features of the material response is described in Sec. II. In particular, details on the derivation of the parameters involved in the assumed exponential plastic hardening law are given. Moreover, the governing equations together with the constitutive model proposed to simulate the deformation process that takes place during the test are presented in Sec. III. This large-strain isotropic elastoplasticity-based formulation includes the definitions of a specific free energy function and plastic evolution equations, which are the basis to derive the stress–strain relationship and a thermodynamically consistent expression for the internal dissipation. The corresponding finite element model is briefly presented in Sec. IV, where a particular treatment of the incompressible plastic flow in order to overcome the well-known volumetric locking in the numerical behavior is discussed. It should be mentioned that this finite element formulation is an alternative approach to existing methodologies dealing with large plastic deformations.

The numerical simulation of the tensile test applied to cylindrical specimens of the just-mentioned aluminum alloys is separately performed in Sec. V. The results obtained with the proposed formulation are validated with the corresponding experimental measurements. Aside from the engineering stress–strain curve, different results at the section undergoing extreme necking are specifically analyzed: ratio of current to initial diameter in terms of the elongation and both load and mean true axial stress vs logarithmic strain. Furthermore, computed nonuniform stress components and effective plastic deformation contours at the fracture stage are also shown confirming the strong influence of the necking formation in the material response. Finally, scanning-electronic-microscopy (SEM) images of the fracture surface are presented in order to qualitatively assess the combined ductile/fragile response of the three studied alloys.

II. Experimental Procedure

The experimental procedure adopted in this work to characterize the mechanical behavior of a material consisted of the following steps:

1) Step one is the selection of the material and the specimen to be tested according to the American Society for Testing and Materials (ASTM) standards.[9] The chosen materials are the aluminum alloys 7075 T7351, 7050 T7451, and 2024 T3 considering cylindrical specimens with a nominal diameter of 9 mm as sketched in Fig. 1. The distance between the two black markers denotes the initial extensometer length taken as 50 mm. A nearly linear gradual reduction in diameter is considered in order to trigger the necking development, which has to take place approximately at the middle of the extensometer length. This tapered profile fits the ASTM standards because the difference between the maximum and minimum diameter values (9 and 8.95 mm, respectively) existing in the extensometer length is lower than 1%.

Before being used in the just-mentioned applications, different heat treatments are carried out in these alloys in order to obtain higher mechanical properties such as yield strength, hardness, and ultimate tensile stress. Specifically, the heat treatment of the 7075 T7351 alloy consists of a solution treatment followed by a quenching stage, an artificial aging (6–8 h at 102–113°C and 6–8 h at

---

Received 10 May 2002; revision received 30 August 2003; accepted for publication 14 September 2003.

*Associate Professor, Departamento de Ingeniería Mecánica, Av. Bdo. O'Higgins 3363; dcelenta@lauca.usach.cl.

†Associate Professor, Departamento de Ingeniería Metalúrgica, Av. Bdo. O'Higgins 3363.

Table 1 Analysis of a cylindrical tension specimen: average chemical composition (% in weight) for the studied aluminum alloys

Element	7075 T7351	7050 T7451	2024 T3
% Al	Bal.	Bal.	Bal.
% Cu	1.55	2.08	4.52
% Mg	2.52	2.07	1.55
% Zn	5.8	6.53	0.0404
% Si	0.0866	0.0244	0.0687
% Fe	0.314	0.0674	0.335
% Ti	0.0334	0.0440	0.0289
% Mn	0.0356	0.00687	0.586
% Cr	0.189	0.00283	0.00450

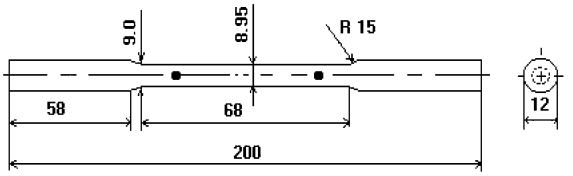

Fig. 1 Analysis of a cylindrical tension specimen: geometry (initial extensometer length = 50 mm).

171–182°C), and, finally, a stress relief by a controlled elongation (0.5 to 3%). The heat treatment of the 7050 T7451 alloy corresponds to a solution heating (70–480°C), a quenching in water (32–38°C) followed by an artificial aging (4–5 h at 110°C, 4–5 h at 116–127°C, 3 h at 152–163°C, and 6 h at 171–182°C), and, again, a stress relief by a controlled elongation (0.5 to 3%). Moreover, the heat treatment of the 2024 T3 alloy starts with a solution treatment, followed by a quenching in water (32–38°C) and a cold working with natural ageing (more than 96 h at 20°C). In general, the improvement of the mechanical properties of these alloys is achieved by the precipitation of small particles, which are totally incoherent with the matrix, because of the supersaturation obtained after the quenching. The stoichiometry of these particles is, for example, (Fe,Mn)Al_6 for the 7075 T7351 alloy and $CuMgAl_2$ in the case of the 2024 T3 alloy. It should be additionally mentioned that for the 7075 T7351 and 7050 T7451 alloys a high stress corrosion resistance is obtained with these treatments.[10]

2) Step two is the chemical characterization to check an adequate composition according to the selected material. This routine task is carried out by means of an optical spectrometer. The average chemical composition for the studied aluminum alloys is shown in Table 1.

3) Mechanical tensile test is the third step. The engineering stress–strain curves obtained with five specimens considering a load cell speed of 2.5 mm/min (value within the range specified by the ASTM standards) are plotted in Fig. 2. As usual, the engineering stress is defined as P/A_0, where P is the axial load and A_0 is the initial transversal area with diameter D_0, and the engineering strain or elongation is computed as $(L–L_0)/L_0$, with L and L_0 being the current and initial extensometer lengths, respectively. As can be seen, the 7075 T7351 and 7050 T7451 alloys exhibit similar responses while lower stresses with a larger ductility are found for the 2024 T3 alloy. At the beginning of the deformation process, the materials behave elastically. In particular, the three alloys present a similar maximum elastic strain of approximately 0.7%. After the yield strength is reached, the plastic hardening begins, and the load increases up to a maximum value for a specific elongation. This point has been found to be different for each alloy. Then, the load decreases because the effect of the reduction of the transversal area at the necking zone is stronger than that of the hardening mechanism (diffuse necking has been found in all cases). The average measured values for the Young's modulus E, yield strength, maximum engineering stress, and elongations at the maximum load and at the fracture stage for the studied alloys are summarized in Table 2. The final extensometer length and diameter at the necking zone of the specimens are also shown in Table 2.

Table 2 Analysis of a cylindrical tension specimen: average experimentally measured material properties and final dimensions for the studied aluminum alloys

Property	7075 T7351	7050 T7451	2024 T3
Young's modulus E, MPa	80,000	76,950	72,580
Yield strength (elongation: 0.2%), MPa	450	470	354
Maximum engineering stress, MPa	516	533	459
Elongation at the maximum load, %	6.5	5	12
Elongation at the fracture stage, %	9	11	15
Hardening coefficient A^p, MPa	700	740	706
Hardening exponent n^p	0.0935	0.0954	0.1489
Final extensometer length, mm	54.5	55.5	57.5
Final diameter at the necking zone, mm	8.05	7.50	7.62

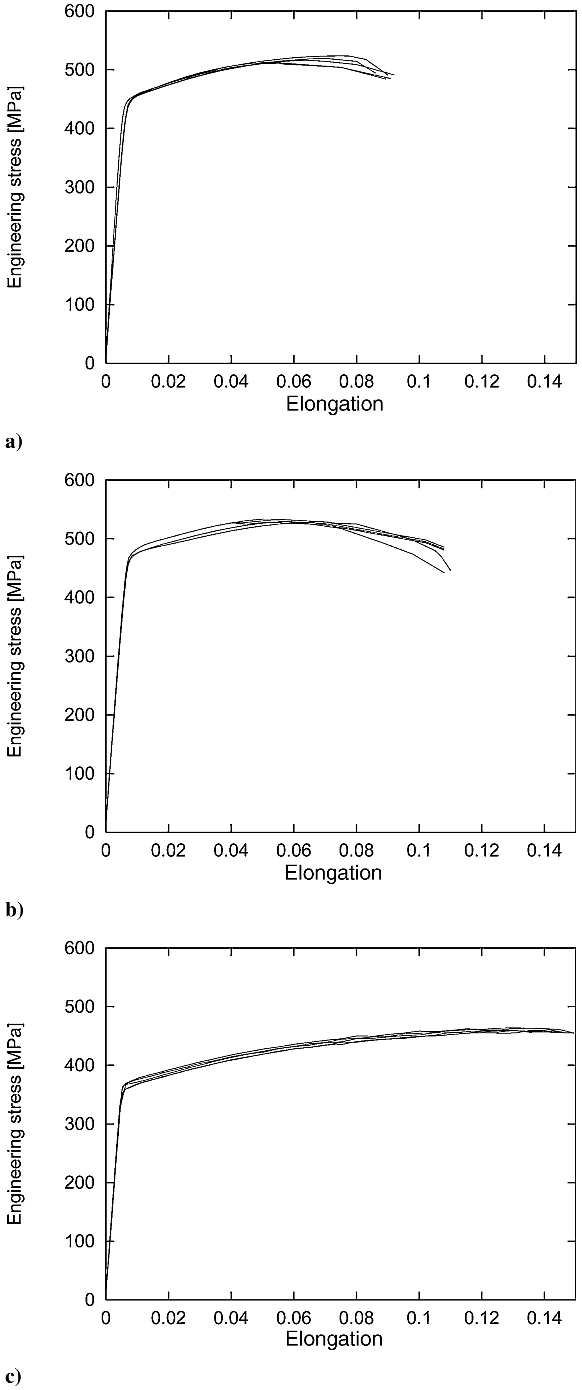

Fig. 2 Analysis of a cylindrical tension specimen: experimental stress–strain curves obtained with five specimens considering a load cell speed of 2.5 mm/min for a) 7075 T7351, b) 7050 T7451, and c) 2024 T3 aluminum alloys.

Table 3 Analysis of a cylindrical tension specimen: correction factor for the stress distribution at the neck[2]

Correction factor f_B	$\ln(A_0/A)$
1.000	0.0
1.000	0.1
0.978	0.2
0.957	0.3
0.938	0.4
0.921	0.5

4) Characterization of the plastic behavior is the last step. At high levels of elongation, the stress and strain distributions are no longer uniform along the specimen because of the necking formation. Therefore, the stress–strain curve of Fig. 2 cannot provide a proper description of the physical phenomena involved in the test. Following the procedure proposed by Bridgman,[2] the mechanical response can be adequately described by an alternative stress–strain curve defined in terms of the mean equivalent stress $\bar{\sigma}_{\mathrm{eq}}$ vs an equivalent deformation $\varepsilon_{\mathrm{eq}}$ (composed of an elastic and plastic contributions) respectively given by $\bar{\sigma}_{\mathrm{eq}} = f_B P/A$ and $\varepsilon_{\mathrm{eq}} = \bar{\sigma}_{\mathrm{eq}}/E + \varepsilon_p$, where $f_B(\varepsilon_p) \leq 1$ is a known correction factor applied to the mean true axial stress P/A (Table 3), A is the current transversal area at the necking zone, $\varepsilon_p = \ln(A_0/A) = -2\ln(D/D_0)$ is the logarithmic deformation, and D is the current diameter of the neck. As can be seen, D is the additional variable to be measured in order to obtain such stress–strain relationships. Figure 3 shows for the studied aluminum alloys the $\bar{\sigma}_{\mathrm{eq}} - \varepsilon_{\mathrm{eq}}$ average experimental data for four specimens and the potential correlation $\bar{\sigma}_{\mathrm{eq}} = A^p \varepsilon_{\mathrm{eq}}^{n^p}$ derived from them, where A^p and n^p are the hardening parameters. These two constants involved in such correlation (see also Table 2) are assumed to define the material hardening behavior (strain rates effects are neglected because of the very low load cell velocity considered in the tests) described by an isotropic strain hardening law shown in the next section.

The curves and parameters obtained in this experimental procedure are the basic data for the numerical simulation and experimental validation presented in Sec. V.

III. Governing Equations and Constitutive Model

The local governing equations describing the evolution of an assumed quasi-static isothermal process (i.e., that with negligible inertia effects and identically fulfilled energy balance) can be expressed by the continuity equation, the equation of motion, and the dissipation inequality (all of them valid in $\Omega x \Upsilon$, where Ω is the spatial configuration of a body and Υ denotes the time interval of interest with $t \in \Upsilon$) respectively written in a Lagrangian description as

$$\rho J = \rho_0 \tag{1}$$

$$\nabla \cdot \boldsymbol{\sigma} + \rho \boldsymbol{b}_f = 0 \tag{2}$$

$$D_{\mathrm{int}} \geq 0 \tag{3}$$

together with appropriate conditions and an adequate constitutive relation for the Cauchy stress tensor $\boldsymbol{\sigma}$ (which is symmetric for the nonpolar case adopted in this work). In these equations, ρ is the density, J is the determinant of the deformation gradient tensor $\boldsymbol{F}(\boldsymbol{F}^{-1} = \mathbf{1} - \nabla \boldsymbol{u}$, where $\mathbf{1}$ is the unity tensor, ∇ is the spatial gradient operator, and $\boldsymbol{u}$ is the displacement vector), the subscript 0 applied to a variable denotes its value at the initial configuration $\boldsymbol{\Omega}_0$, $\boldsymbol{b}_f$ is the specific body force vector, and D_{int} is the internal dissipation that imposes restrictions over the constitutive model definition. In this framework, a specific Helmholtz free energy function ψ, assumed to describe the material behavior during the deformation process, can be defined in terms of some thermodynamic state variables chosen in this work as the Almansi strain tensor $\boldsymbol{e}[\boldsymbol{e} = \frac{1}{2}(\mathbf{1} - \boldsymbol{F}^{-T} \cdot \boldsymbol{F}^{-1})]$, where T is the transpose symbol and a set of n_{int} phenomenological internal variables $\boldsymbol{\alpha}_k$ (usually governed by rate equations with $k = 1, \ldots, n_{\mathrm{int}}$) accounting for the nonreversible effects.[6,8,11] This free energy definition, based on the Doyle–Ericksen's approach,[12] is only valid for small elastic strains and isotropic material response, both assumptions being normally accepted for metals and other materials. Invoking Coleman's method,[13] the following relationships are obtained:

$$\boldsymbol{\sigma} = \rho \frac{\partial \psi}{\partial \boldsymbol{e}}, \qquad D_{\mathrm{int}} = \boldsymbol{q}_k^* \frac{\mathrm{D}\boldsymbol{\alpha}_k}{\mathrm{D}t}$$

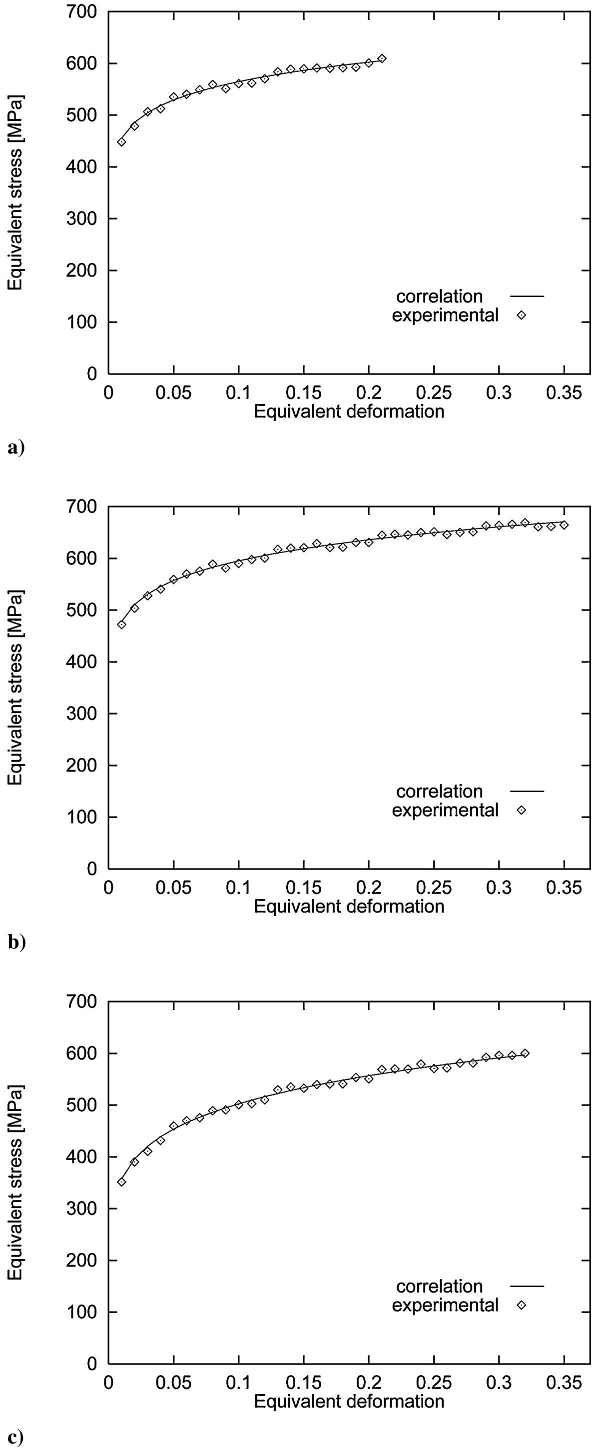

Fig. 3 Analysis of a cylindrical tension specimen: mean equivalent stress vs equivalent deformation obtained with four specimens considering a load cell speed of 2.5 mm/min for a) 7075 T7351, b) 7050 T7451, and c) 2024 T3 aluminum alloys. (The hardening parameters of the respective potential correlations can be found in Table 2.)

where

$$\boldsymbol{q}_k = -\rho_0 \frac{\partial \psi}{\partial \boldsymbol{\alpha}_k}$$

are the conjugate variables of $\boldsymbol{\alpha}_k$ and, according to the nature of each internal variable, the symbols $*$ and $\mathrm{D}(\cdot)/\mathrm{D}t$ appearing in the preceding expressions respectively indicate an appropriate multiplication and a time derivative satisfying the principle of material frame indifference.[14]

It is seen that the definitions of $\psi = \psi(\boldsymbol{e}, \boldsymbol{\alpha}_k)$ and $\mathrm{D}\boldsymbol{\alpha}_k/\mathrm{D}t$ are crucial features of the model in order to derive the constitutive equations just presented.

The internal variables and their corresponding evolution equations are defined in this work within the associate rate-independent plasticity theory context.[7,15] A possible choice is given by the plastic Almansi strain tensor $\boldsymbol{e}^p$ and the effective plastic deformation $\bar{e}^p$ related to the isotropic strain-hardening effect.[6,8,11] The evolution equations for such plastic variables are written as

$$L_v(\boldsymbol{e}^p) = \dot{\lambda} \frac{\partial F}{\partial \boldsymbol{\tau}} \qquad \dot{\bar{e}}^p = \dot{\lambda} \tag{4}$$

where $\boldsymbol{\tau}$ is the Kirchhoff stress tensor ($\boldsymbol{\tau} = J\boldsymbol{\sigma}$), L_v is the well-known Lie (frame-indifferent) derivative, $\dot{\lambda}$ is the rate (or increment in this context) of the plastic consistency parameter computed according to classical concepts of the plasticity theory,[7] and $F = F(\boldsymbol{\sigma}, \bar{e}^p)$ is the yield function governing the plastic behavior of the solid such that no plastic evolutions occur when $F < 0$. A von Mises yield function is adopted:

$$F = \sqrt{3J_2} - C^p \tag{5}$$

where J_2 is the second invariant of the deviatoric part of $\boldsymbol{\tau}$ and C^p is the plastic hardening function given by

$$C^p = A^p \left(\bar{e}_0^p + \bar{e}^p\right)^{n^p} \tag{6}$$

where $\bar{e}_0^p$ is an assumed initial value of $\bar{e}^p$ such that $C^{th} = C^p|_{\bar{e}^p = 0} = A^p \bar{e}_0^{p\,n^p}$ with C^{th} being the yield strength defining the elastic bound of the material prior to further plastic deformation. The hardening material parameters A^p and n^p characterize the plastic behavior in the plastic range, and they are derived, as described in Sec. II, from the experimental-based correlation of the mean equivalent stress vs equivalent deformation curve. Furthermore, in this context the effective plastic deformation rate can be also computed as $\dot{\bar{e}}^p = \sqrt{(\frac{2}{3} \boldsymbol{d}^p : \boldsymbol{d}^p)}$, where $\boldsymbol{d}^p = L_v(\boldsymbol{e}^p)$ is the plastic contribution of the rate-of-deformation tensor $\boldsymbol{d}$ given by $\boldsymbol{d} = \frac{1}{2}(\boldsymbol{\nabla v} + \boldsymbol{v\nabla})$, where $\boldsymbol{v} = \dot{\boldsymbol{u}}$ is the velocity vector. A consequence of this model is that $tr(\boldsymbol{d}^p) = 0$ (tr is the trace symbol), which reflects the incompressibility nature of the plastic flow that has been physically observed in many metals at moderate pressure levels.[2]

The following specific free energy function $\psi = \psi(\boldsymbol{e} - \boldsymbol{e}^p, \bar{e}^p)$ is proposed:

$$\begin{aligned} \psi &= (1/2\rho_0)(\boldsymbol{e} - \boldsymbol{e}^p) : \boldsymbol{C} : (\boldsymbol{e} - \boldsymbol{e}^p) + (1/\rho_0)(\boldsymbol{e} - \boldsymbol{e}^p) : \boldsymbol{C} : \boldsymbol{\tau}_0 \\ &\quad - \left[1\big/(n^p + 1)\rho_0\right] A^p \left(\bar{e}_0^p + \bar{e}^p\right)^{n^p + 1} + (1/\rho_0) C^{th} \bar{e}^p + \psi_0 \end{aligned} \tag{7}$$

where $\boldsymbol{C}$ is the isotropic elastic constitutive tensor and $\boldsymbol{\tau}_0$ denotes an initial stress field. This last equation is a partially coupled form of defining ψ, which considers the density at the initial configuration according to the simplification of Doyle–Ericksen's approach.[12] However, the elastic/plastic decomposition of ψ can be considered nowadays well established because different versions of it have successfully been used in many engineering applications (for example, see Refs. 3–8, 11, 15, and 16 and references therein). Moreover, the additive decomposition of the Almansi strain tensor is recovered in this context through the multiplicative decomposition of the deformation gradient into elastic and plastic contributions.[6] The description of the fracture and damage phenomena are not included in the proposed specific free energy function given by Eq. (7).

The preceding definitions allow the derivation of the stress–strain law (secant or hyperelastic form for the Cauchy stress tensor) and the expression of the internal dissipation, which are, respectively, given by

$$\boldsymbol{\sigma} = (1/J)[\boldsymbol{C} : (\boldsymbol{e} - \boldsymbol{e}^p) + \boldsymbol{\tau}_0] \tag{8}$$

$$D_{\text{int}} = \boldsymbol{\tau} : L_v(\boldsymbol{e}^p) + (C^p - C^{th})\dot{\bar{e}}^p \geq 0 \tag{9}$$

The tangent form of the stress–strain law stated by Eq. (8) can be obtained by applying standard procedures of the plasticity theory.[7] Although this rate expression is not strictly needed within the present hyperelastic context, its derivation is particularly relevant in the computation of the stiffness matrix appearing in the finite element formulation described in Sec. IV. Finally, the internal dissipation inequality (9) is effectively fulfilled (i.e., both terms are separately nonnegative for every thermodynamic state) owing to the adopted definitions for the plastic evolution equations (4).

IV. Finite Element Formulation

The finite element equations derived from the model just presented are briefly described in this section together with some important features of the numerical strategy used to solve the resulting system of discrete equations.

Following the standard procedures within the finite element framework,[17] the global discretized equilibrium equation including mass conservation can be written in matrix form for a certain time t (or load level for the present quasi-static case) as

$$\boldsymbol{R}_U \equiv \boldsymbol{F}_U - \boldsymbol{F}_\sigma = 0 \tag{10}$$

where $\boldsymbol{R}_U$ is the residual vector, $\boldsymbol{F}_U$ is the external force vector, and $\boldsymbol{F}_\sigma$ denotes the internal force vector. The element expressions of these vectors are given here.

Element vectors in the discretized equilibrium equation:

$$\boldsymbol{F}_U^{(e)} = \int_{\Omega_0^{(e)}} \boldsymbol{N}_U^T \boldsymbol{b}_{F_0} \, \mathrm{d}\Omega_0 + \int_{\Gamma_{\sigma_0}^{(e)}} \mathbf{N}_U^T \bar{\boldsymbol{t}}_0 \, \mathrm{d}\Gamma_{\sigma_0} + \sum_{j=1}^{n_{cU}} \boldsymbol{F}_{cUj}^{(e)}$$

$$\boldsymbol{F}_\sigma^{(e)} = \int_{\Omega_0^{(e)}} \bar{\boldsymbol{B}}^T \boldsymbol{S} \, \mathrm{d}\Omega_0$$

where $\boldsymbol{N}_U$ is the shape function matrix for displacements, $\boldsymbol{b}_{F_0}$ the body force vector at initial configuration Ω_0, $\bar{\boldsymbol{t}}_0$ the traction vector at the boundary $\Gamma_{\sigma_0} \subset \Gamma_0$ ($\Gamma_0 = \partial\Omega_0$), $\boldsymbol{F}_{cU}^{(e)}$ the point force vector at element e with n_{cU} loaded nodes, $\bar{\boldsymbol{B}}$ the strain-displacement matrix for large strains to avoid numerical locking caused by incompressible plastic deformation (see Ref. 11), $\boldsymbol{S} = J\boldsymbol{F}^{-1} \cdot \boldsymbol{\sigma} \cdot F^{-T}$ the second Piola–Kirchhoff stress tensor, and superscript T the transpose symbol.

Note that $\boldsymbol{R}_U$ is computed at the initial configuration using the well-known total Lagrangian approach.[18] In this context, all of the variables involved in $\boldsymbol{R}_U$ have to be transformed to the initial configuration. Moreover, a unconditionally stable generalized midpoint rule algorithm has been used to integrate the plastic rate equations just presented via a return-mapping procedure.[7,18] On the other hand, the Jacobian matrix needed in the Newton–Raphson iterative process is here, where, owing to the strong nonlinearities inherent in the formulation, an approximated but numerically accurate expressions for $\boldsymbol{J}_{UU}$ is considered, where $\boldsymbol{K}_U$ is the so-called stiffness matrix.

Jacobian matrix for the Newton–Raphson iterative procedure:

$$\boldsymbol{J}_{UU} = -\frac{\partial \boldsymbol{R}_U}{\partial \boldsymbol{U}} \cong \boldsymbol{K}_U$$

with

$$\boldsymbol{K}_U^{(e)} = \int_{\Omega_0^{(e)}} \bar{\boldsymbol{B}}^T \frac{\partial \boldsymbol{S}}{\partial \boldsymbol{E}} \bar{\boldsymbol{B}} \, \mathrm{d}\Omega_0 + \int_{\Omega_0^{(e)}} \bar{\boldsymbol{H}}^T \boldsymbol{S} \bar{\boldsymbol{H}} \, \mathrm{d}\Omega_0$$

where $\boldsymbol{U}$ is the nodal displacement vector, $\partial \boldsymbol{S}/\partial \boldsymbol{E}$ the tangent elastoplastic constitutive tensor at initial configuration Ω_0 (E the Green–Lagrange strain tensor), and $\bar{\boldsymbol{H}}$ the strain-displacement matrix for large strains derived by linearization of $\bar{\boldsymbol{B}}$.

In this total Lagrangian approach, the stiffness matrix consists of two terms usually denoted as the material and geometric contributions respectively related to the elastoplastic constitutive behavior and the nonlinear effects of the adopted strain measure.[18]

Although classical spatial interpolations for the displacement field have been considered in Eq. (10), an improved strain-displacement matrix $\bar{\boldsymbol{B}}$, previously proposed by Celentano[11] and checked in problems involving moderate deformations, is also employed in this work in order to overcome the volumetric locking effect on the numerical solution when incompressible plastic flows are studied. The performance of this methodology is now tested in a large strain situation like the necking process of a cylindrical tension specimen described next. Based on the deformation gradient standard decomposition into deviatoric and volumetric parts and assuming a selective numerical integration for the volumetric part of $\boldsymbol{F}$, the $\bar{\boldsymbol{B}}$ matrix is obtained by linearization of the Green–Lagrange strain tensor. The expressions of this matrix for the two-dimensional, axisymmetric and three-dimensional cases can be found in the mentioned reference. The $\bar{\boldsymbol{B}}$ matrix has not a sparse structure. Nevertheless, the additional computations required at element level were found not to significantly increase the CPU times in comparison with the standard sparse strain-displacement matrix. This methodology is an alternative approach to the assumed strain mixed finite element method developed by Simo and Armero[4] in which a sparse gradient operator is obtained with the drawback of computing and storing, at element level, enhanced strain parameters defined in such context. Note that these last operations are not needed in the present $\bar{\boldsymbol{B}}$ algorithm, and, hence, a simple computational implementation of it can be attained.

V. Numerical Simulation and Experimental Validation

The finite element formulation just presented is used to simulate the material behavior of the aluminum alloys 7075 T7351, 7070 T7451, and 2024 T3 during the tensile tests described in Sec. II. According to the experimental measurements performed during these tests, the material properties considered in the numerical analysis for such alloys are shown in Table 4. The spatially nonuniform finite element mesh shown in Fig. 4 has been chosen in order to correctly describe the large stress and deformation gradients expected in the necking zone. Assuming axisymmetry, a fourth of the specimen is discretized with a height of 25 mm (half of the initial extensometer length) and a linear radius variation along the bar according to the geometry specifications depicted in Fig. 1, where $\boldsymbol{U}_{\text{top}}$ denotes the axial displacement imposed at the top boundary up to a value, which corresponds, for each alloy, to the respective fracture elongation (see Table 2). Moreover, the analysis is performed with $\boldsymbol{b}_f = 0$ and $\boldsymbol{\tau}_0 = 0$.

The main objective of the present analysis is to validate the predictions of the proposed formulation with the available experimental data obtained in the tensile tests in order to achieve an adequate mechanical characterization of the studied materials, which allow, in turn, the comparison and discussion of their distinctive responses. To this end, similar results are separately presented below for each alloy. Firstly, model predictions of the engineering stress–strain relationship and other results at the necking section are contrasted with the corresponding average experimental measurements. Then, computed stress components and effective plastic deformation distributions at the fracture stage are shown. Finally, SEM images of the fracture surface obtained in a scanning electronic microscope using secondary electrons over such surface are qualitatively studied, where, besides, a chemical analysis by energy dispersive x-ray analysis (EDAX) was used to identify the chemical composition of some particles found in these materials.

Table 4 Analysis of a cylindrical tension specimen: material properties considered in the simulation for the studied aluminum alloys

Property	7075 T7351	7050 T7451	2024 T3
Young's modulus E, MPa	80,000	76,950	72,580
Poisson's ratio ν	0.3	0.3	0.3
Yield strength C^{th}, MPa	450	470	354
Hardening coefficient A^p, MPa	700	740	706
Hardening exponent n^p	0.0935	0.0954	0.1479

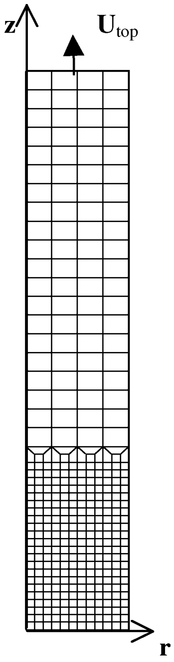

Fig. 4 Analysis of a cylindrical tension specimen: finite element mesh used in the analysis composed of 360 four-noded isoparametric elements.

A. 7075 T7351 Aluminum Alloy

Figure 5 shows the engineering stress–strain relationship and some results at the section undergoing extreme necking: the radii relation vs the elongation in the necking zone together with the load and mean true axial stress both against the logarithmic deformation. An overall good agreement between the numerical predictions and the average experimental values can be observed in these curves. In particular, the elastic region as well as the beginning of the hardening process are realistically described by the simulation. Although some small discrepancies in the engineering stress, load and mean true axial stress appear at higher levels of deformation, such differences are approximately bounded within the experimental uncertainty range. The experimentally measured load decreases from an elongation of 6.5%, which is equivalent to a logarithmic deformation ε_p of 9.0% onwards. (The corresponding numerical values for such deformations are 6.8 and 9.4%, respectively.) However, the mean true axial stress continues increasing until the fracture stage where a big amount of plastic hardening can be appreciated. This fact confirms that a geometrical instability occurs (instead of a constitutive instability) because, as already commented in Sec. II, the effect on the stress caused by the reduction of the transversal area at the necking zone predominates over the material hardening. At high level of deformations, the regions of the specimen outside the necking zone are being elastically unloaded. Moreover, note that the well-known simplified relationship,[19] stating that the related logarithmic deformation at the point of maximum load has to be equal to the hardening exponent, is approximately verified (see Table 2).

The ratio of current to initial diameter in terms of the elongation starts with a linear relationship, reflecting uniform distributions of stresses and strains, which presents an approximate slope of 0.5 caused by the incompressibility nature of the plastic flow. The same situation is kept up to an elongation of 6.5%, which corresponds, as just mentioned, to the point of maximum load (see Table 2). Afterward, a sudden reduction of the diameter takes place causing the necking formation and, hence, nonhomogeneous stress and strain

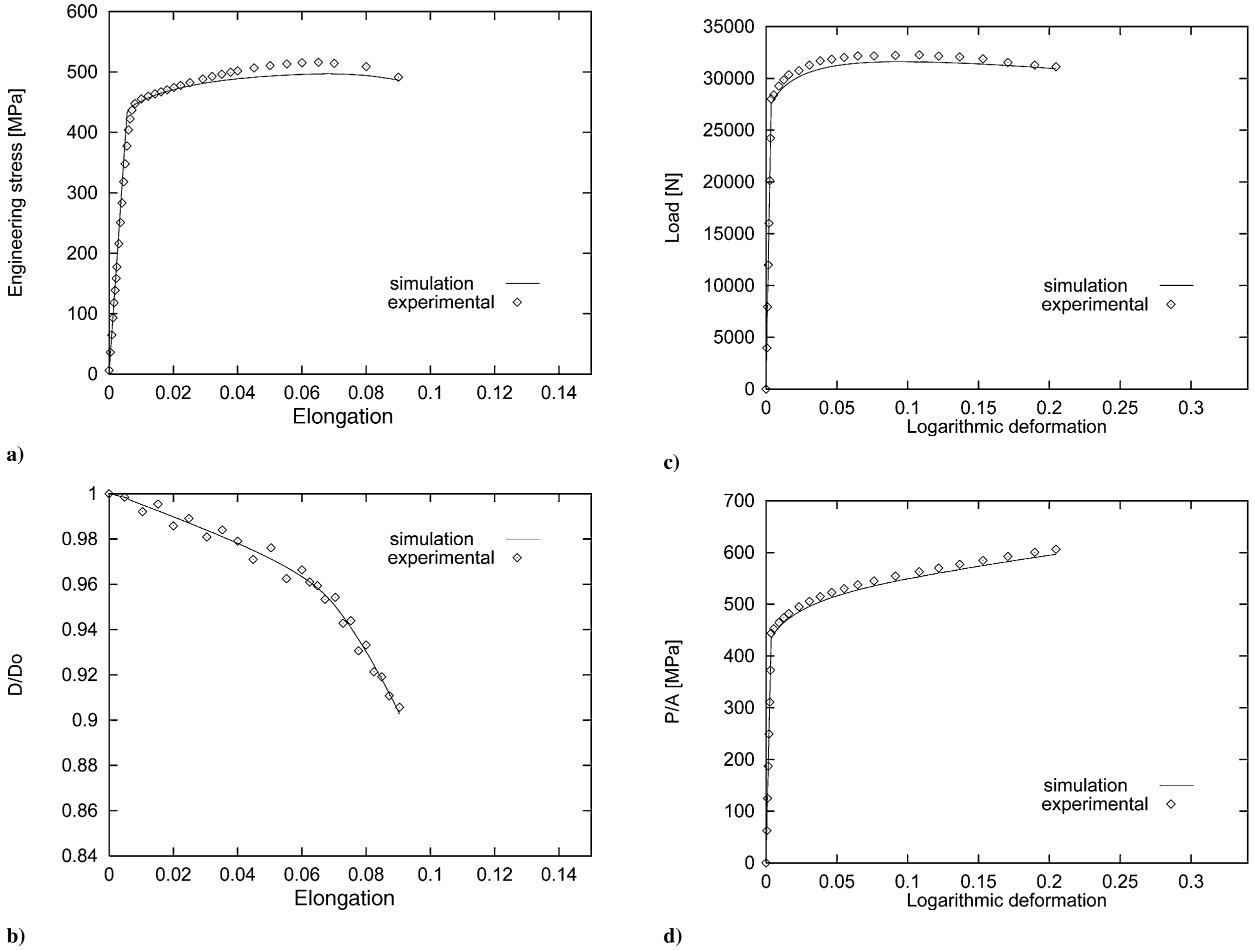

a)

b)

c)

d)

Fig. 5 Analysis of a 7075 T7351 aluminum alloy cylindrical tension specimen: a) engineering stress–strain relationship, with results at the section undergoing extreme necking; b) ratio of current to initial diameter vs axial elongation; c) load vs logarithmic deformation; and d) mean true axial stress vs logarithmic deformation.

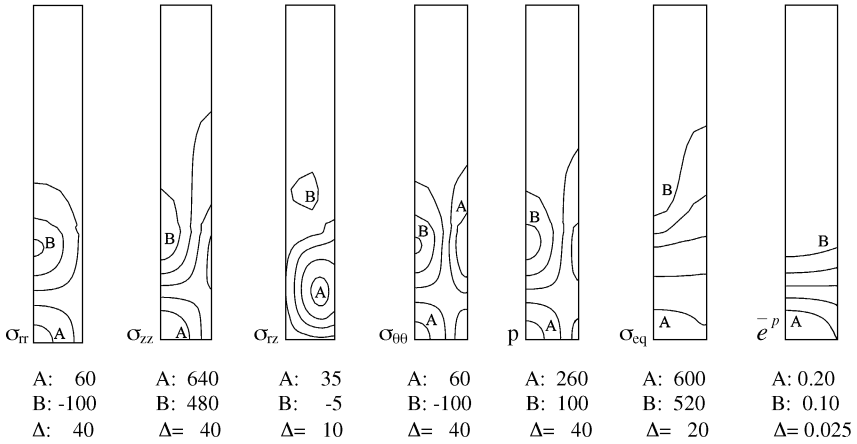

Fig. 6 Analysis of a 7075 T7351 aluminum alloy cylindrical tension specimen: stress (in MPa) and effective plastic deformation contours at the end of the analysis corresponding to the fracture stage for an elongation of 9%.

distributions along the specimen. As can be seen, the numerical results fit very well the experimental ones during the whole test.

Different stress components [radial, axial, shear, and hoop components of $\boldsymbol{\sigma}$ together with the pressure $p = \frac{1}{3} tr(\boldsymbol{\sigma})$ and the equivalent stress σ_{eq} given by $\sqrt{(3J_2)}$] and effective plastic deformation contours at the end of the analysis can be found in Fig. 6. Nonuniform distributions are clearly obtained as a result of the complex deformation pattern of the neck. As expected, the maximum values of σ_{eq} and consequently of $\bar{e}^p$ are concentrated in the neck. Note that values around 0.09 of effective plastic deformation mainly found at the rear part of the specimen indicate the level of uniform deformation experienced until the maximum load is reached (see Fig. 5). The neck formation even induces the development of low pressures at the center of the bar. (This fact has also been pointed out by Armero and Simo[5] and Goicolea et al.[8] in the tension analysis of other materials.) Furthermore, some assumptions considered in the analytical study of Bridgman[2] at the neck are ratified by the simulation, for example, σ_{eq} and $\bar{e}^p$ are approximately constant, σ_{rr} and

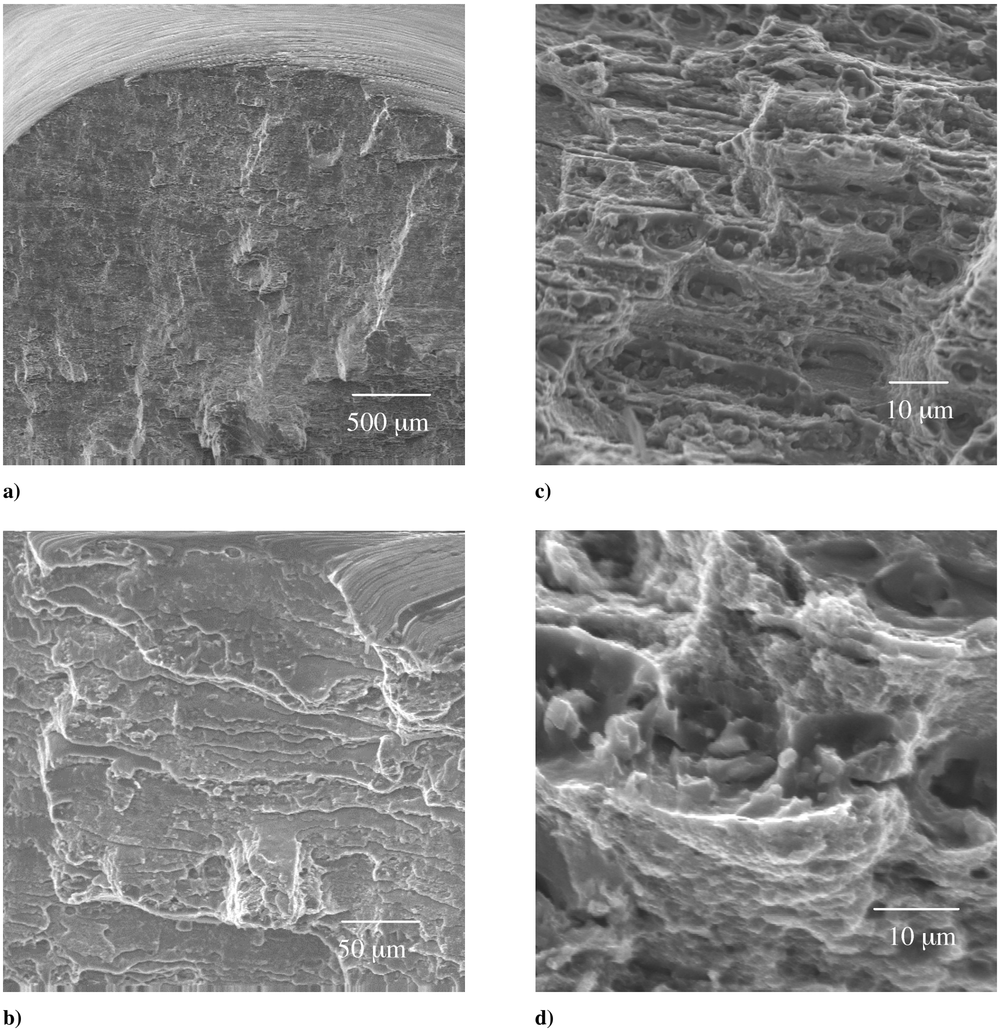

a) c) b) d)

Fig. 7 Analysis of a 7075 T7351 aluminum alloy cylindrical tension specimen. SEM images of the fracture surface: a) 50×, b) 500×, c) 1500×, and d) 2000×.

$\sigma_{\theta\theta}$ present a strong variation, but the condition $\sigma_{rr} \approx \sigma_{\theta\theta}$ is fulfilled, $\sigma_{zz} \approx \sigma_{\mathrm{eq}} + \sigma_{rr} > \sigma_{\mathrm{eq}}$, which explains the need to correct the stress distribution (see Table 3), $p \approx \sigma_{\mathrm{eq}}/3 + \sigma_{rr}$, and $e_{zz} \approx -2e_{rr}$ up to the maximum load and $e_{rr} \approx e_{\theta\theta}$ during the whole test.

Figure 7 shows SEM images of the fracture surface at different magnifications. A general view of the fracture surface can be appreciated in Fig. 7a, where zones of high and low plastic deformation are apparent in Fig. 7b. In Figs. 7c and 7d it is possible to observe a banded structure related to the cold rolling previously experienced by this alloy. Furthermore, a great amount of particles can be appreciated on the fracture surface. The EDAX analysis of these particles revealed that their stoichiometry correspond to (Fe,Mn)Al_6. According to fracture mechanics,[1,19] the fracture starts in these particles through the mechanisms of nucleation, growth, and coalescence of cavities. This theory can be confirmed by the presence of voids on the fracture surface. In fact, the lowest cohesion energy levels occur precisely in the interface of these particles with the matrix. The presence of small cracks on the fracture surface together with zones of low plastic deformation, both clearly observable in Fig. 7d, explains the combined ductile-fragile nature of the fracture phenomenon that develops in this alloy.

B. 7050 T7451 Aluminum Alloy

As in the preceding analysis, Fig. 8 shows experimental and numerical results corresponding to the engineering stress–strain relationship, the radii relation vs the elongation in the necking zone, and the load and mean true axial stress both against the logarithmic deformation at the neck, where, once more, a good experimental validation of the numerical predictions can be seen. Although the mechanical behaviors of the 7075 T7351 and 7050 T7451 alloys are in general quite similar, the latter develops larger amounts of deformation, characterized by lower values of D/D_0 and consequently higher logarithmic strains in spite of the relatively low final elongation of 11%, during the tensile process. This fact also implies an increase of the different components of the stress tensor at the fracture stage as a result of the larger hardening effect involved in this case (Fig. 9). Moreover, the numerically predicted elongation and logarithmic deformation at the maximum load, respectively, given by 7.0 and 9.5% reasonably adjust the corresponding experimental values of 5 and 10%.

The SEM images of the fracture surface for the 7050 T7451 alloy shown in Fig. 10 present the same features as those already commented for the 7075 T7351 alloy, that is, its ductile-brittle fracture response confirmed by the presence of small cracks, many zones of low plastic deformation, and little regions of ductile fracture.

C. 2024 T3 Aluminum Alloy

As can be seen in Fig. 11, the 2024 T3 alloy develops, in comparison with the 7075 T7351 and 7050 T7351 alloys (see Figs. 5 and 8, respectively), a more ductile response given by larger elongations at the maximum load and fracture stages (see also Table 2). However, its final values of D/D_0 and logarithmic strains are slightly lower than those observed for the 7050 T7451 alloy denoting, as shown in Fig. 12, a more uniform distribution of the plastic deformation for the 2024 T3 alloy (compare the respective $\bar{e}^p$ contours of Figs. 9 and 12). The stress levels achieved by this alloy are close to

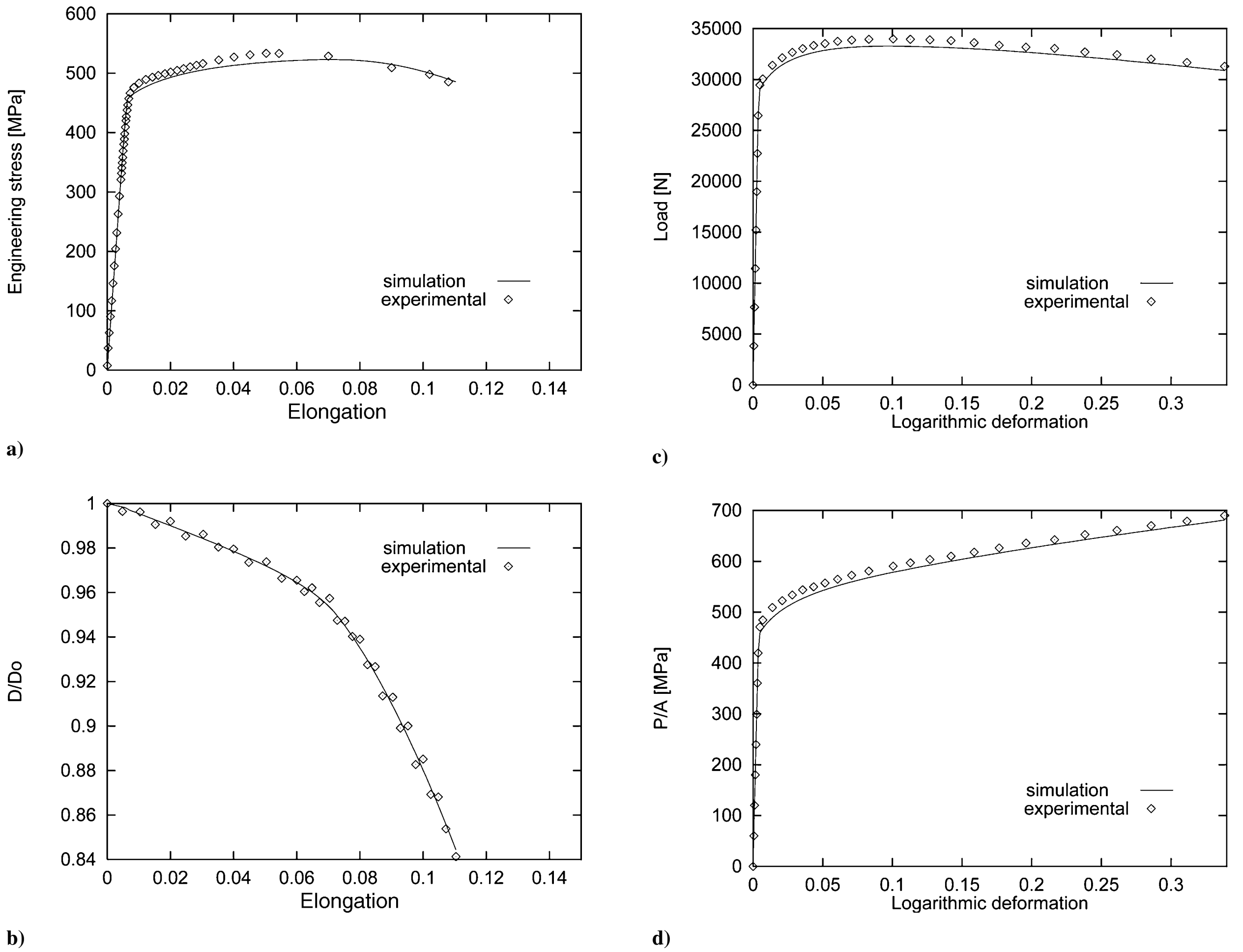

Fig. 8 Analysis of a 7050 T7451 aluminum alloy cylindrical tension specimen: a) engineering stress–strain relationship, with results at the section undergoing extreme necking; b) ratio of current to initial diameter vs axial elongation; c) load vs logarithmic deformation; and d) mean true axial stress vs logarithmic deformation.

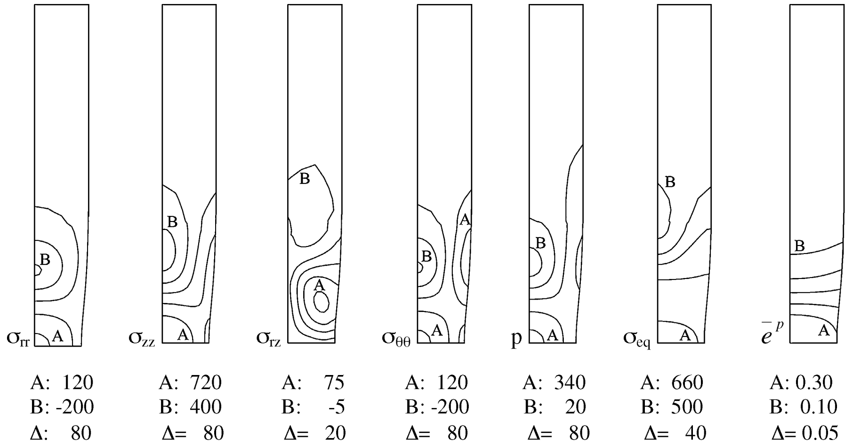

Fig. 9 Analysis of a 7050 T7451 aluminum alloy cylindrical tension specimen: stress (in MPa) and effective plastic deformation contours at the end of the analysis corresponding to the fracture stage for an elongation of 11%.

those observed for the 7075 T7351 alloy, which are, as already commented, smaller than those corresponding to the 7050 T7451 alloy. This fact makes clear the relevant hardening effect experienced by the 2024 T3 alloy in spite of its relatively low yield strength (see Table 2). Moreover, very similar experimental and simulated deformations at the maximum load have been obtained (respectively expressed by elongations of 12 and 11.7% and logarithmic strains of 14 and 14.4%).

The SEM images of Fig. 13 confirm the presence of a more ductile fracture in the 2024 T3 alloy in contrast to the kind of fracture observed for the 7075 T7351 and 7050 T7451 alloys (see Figs. 7 and 10, respectively). The obtained stoichiometry of the particles existing in the voids observed in Fig. 13b has been, by EDAX analysis, $CuMgAl_2$. As in the earlier analyzed alloys, the fracture begins in these particles via the same mechanisms. Although small zones of brittle fracture can be seen, the relatively large plastic deformations

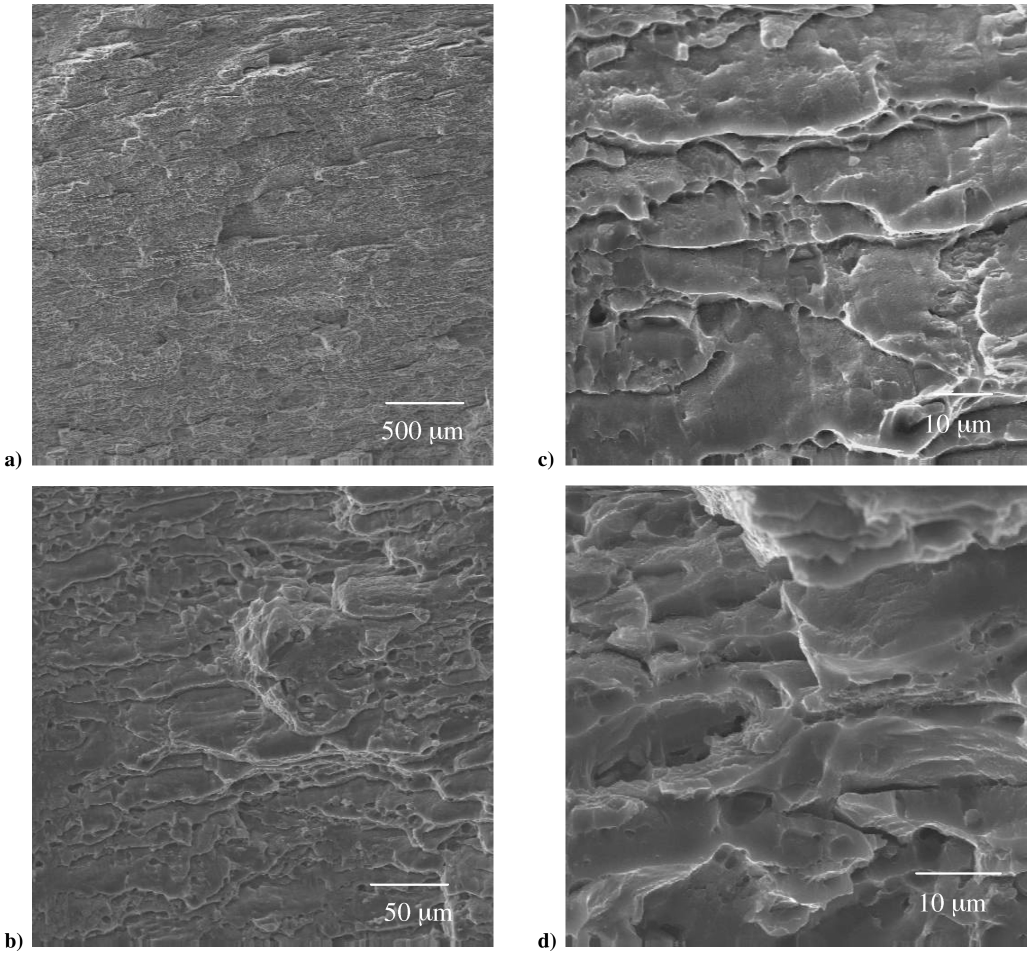

Fig. 10 Analysis of a 7050 T7451 aluminum alloy cylindrical tension specimen. SEM images of the fracture surface: a) 50×, b) 500×, c) 1500×, and d) 2000×.

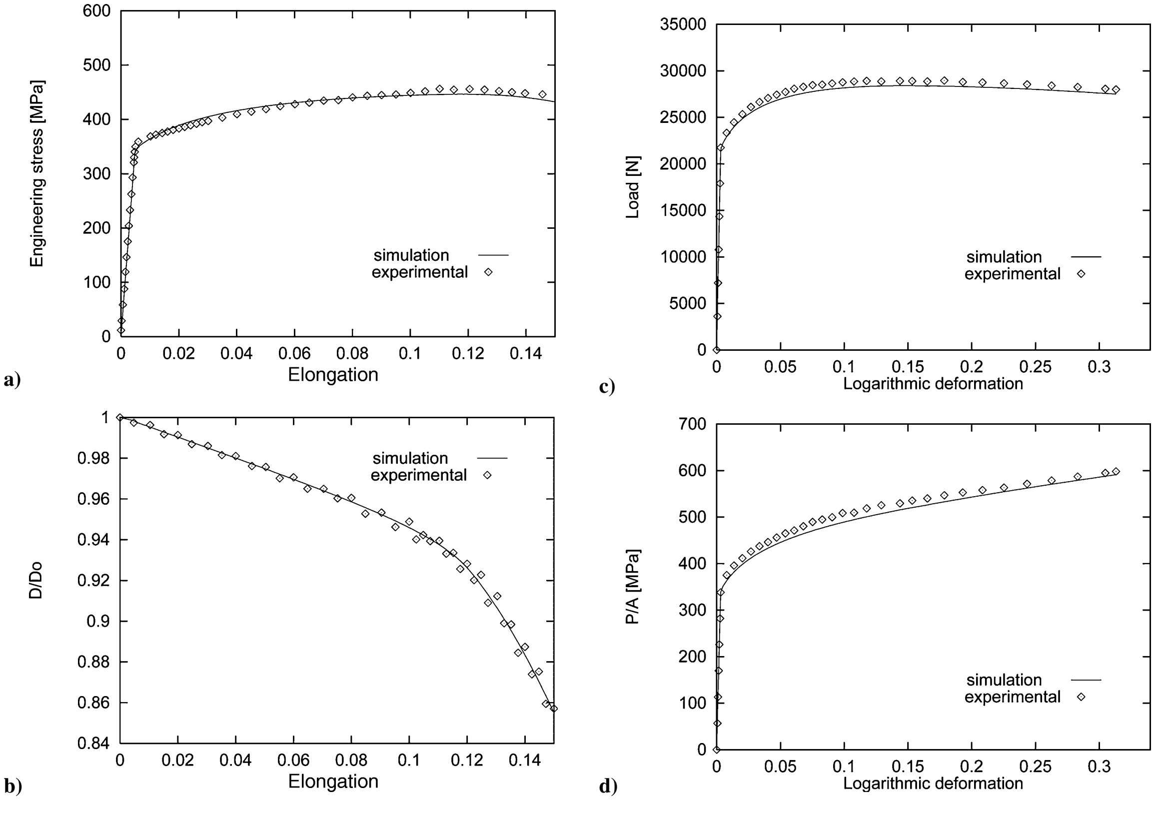

Fig. 11 Analysis of a 2024 T3 aluminum alloy cylindrical tension specimen: a) engineering stress–strain relationship, with results at the section undergoing extreme necking; b) ratio of current to initial diameter vs axial elongation; c) load vs logarithmic deformation; and d) mean true axial stress vs logarithmic deformation.

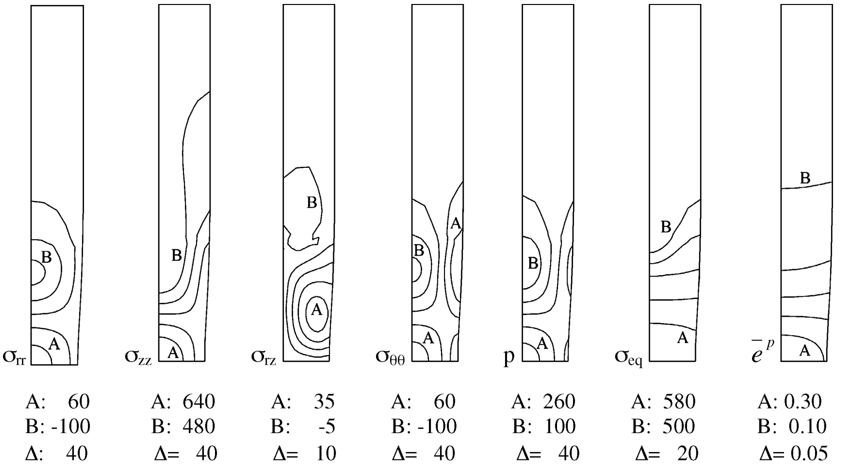

Fig. 12 Analysis of a 2024 T3 aluminum alloy cylindrical tension specimen: stress (in MPa) and effective plastic deformation contours at the end of the analysis corresponding to the fracture stage for an elongation of 15%.

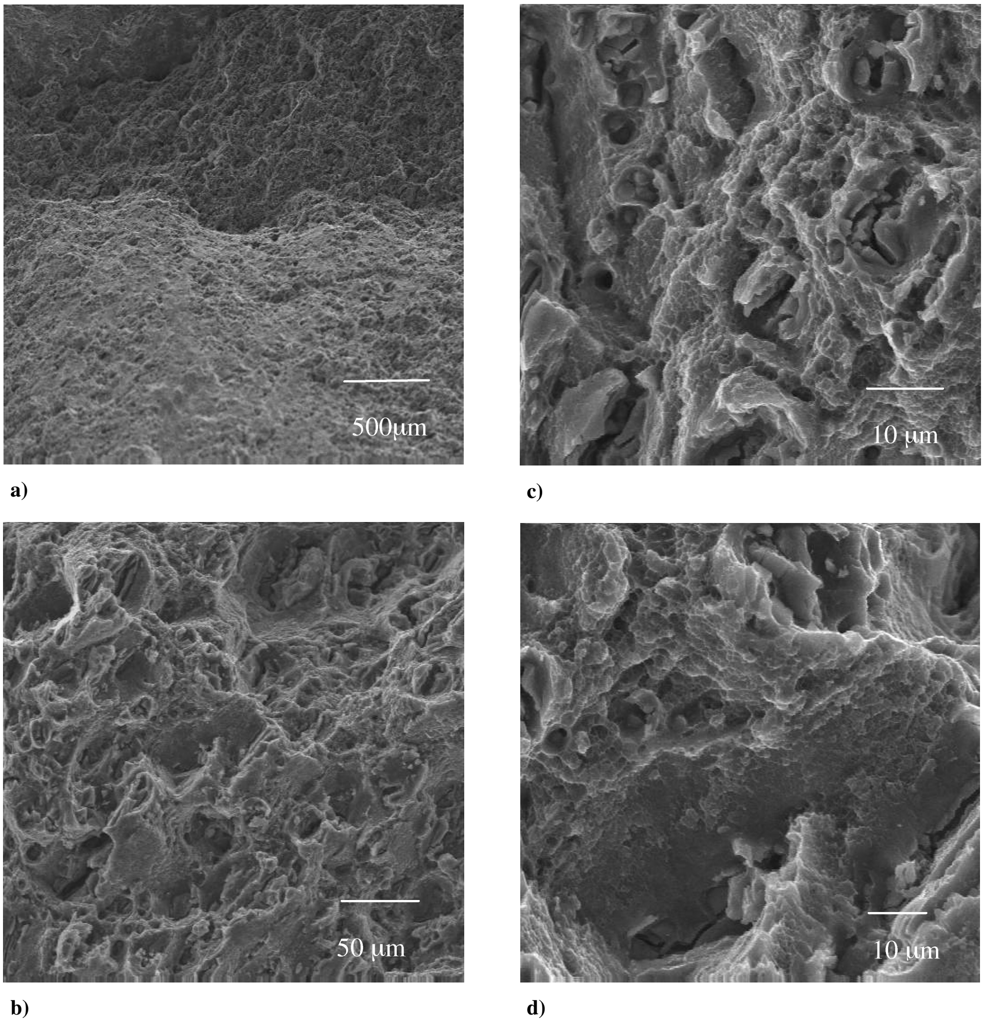

a) c) b) d)

Fig. 13 Analysis of a 2043 T3 aluminum alloy cylindrical tension specimen. SEM images of the fracture surface: a) 50×, b) 500×, c) 1500×, and d) 2000×.

typically found in ductile fracture responses predominate in this alloy.

VI. Conclusions

Experimental and numerical analyses of the mechanical behavior occurring in cylindrical specimens during the standard tensile test applied to three extensively used aeronautical aluminum alloys have been presented. A characterization of the material response has been first performed in order to obtain the stress–strain curve and the diameter evolution at the neck. From these data, elastic and hardening parameters have been derived applying a well-established methodology. Moreover, a finite element large-strain elastoplasticity-based formulation has been proposed and used to simulate the tensile deformation process. Some original features of such formulation have also been discussed.

The numerical results obtained with this formulation have been satisfactorily validated with the related experimental measurements.

In particular, the engineering stress-strain relationship, the diameter evolution of the neck, and the mean true axial stress history during the test have been very well predicted by the simulation. Although some discrepancies between the numerical and experimental data have been observed, the overall trends have been properly captured by the model.

Acknowledgments

The supports provided by the Chilean Council of Research and Technology CONICYT (FONDECYT Project 1020026) and the Department of Technological and Scientific Research at the University of Santiago de Chile are gratefully acknowledged. The authors express their appreciation to the Aeronautical Technical Academy at Santiago de Chile for the provision of experimental facilities.

References

[1] Nádai, A., *Theory of Flow and Fracture of Solids*, McGraw–Hill, London, 1950, Chap. 1.

[2] Bridgman, P., *Studies in Large Plastic and Fracture*, McGraw–Hill, London, 1952, Chap. 8.

[3] Wriggers, P., Miehe, C., Kleiber, M., and Simo, J., "On the Coupled Thermo-Mechanical Treatment of Necking Problems via Finite-Element-Method," *Proceedings of COMPLAS II*, edited by R. Owen, E. Hinton, and E. Oñate, Pineridge Press, Swansea, Wales, U.K., 1989, pp. 527–542.

[4] Simo, J., and Armero, F., "Geometrically Non-Linear Enhanced Strain Mixed Methods and the Method of Incompatible Modes," *International Journal for Numerical Methods in Engineering*, Vol. 33, 1992, pp. 1413–1449.

[5] Armero, F., and Simo, J., "A Priori Stability Estimates and Unconditionally Stable Product Formula Algorithms for Non-Linear Coupled Thermoplasticity," *International Journal of Plasticity*, Vol. 9, 1993, pp. 149–182.

[6] García Garino, C., and Oliver, J., "A Numerical Model for Elastoplastic Large Strain Problems. Fundamentals and Applications," *Proceedings of COMPLAS III*, edited by R. Owen, E. Oñate, and E. Hinton, Pineridge Press/CIMNE, Swansea, Wales, U.K., 1993, p. 117.

[7] Simo, J., *Topics on the Numerical Analysis and Simulation of Plasticity, Handbook of Numerical Analysis*, Vol. 3, Elsevier Science, Amsterdam, 1995, Chaps. 1–4.

[8] Goicolea J., Gabaldón, F., and García Garino, C., "Analysis of the Tensile Test Using Hypo and Hyperlastic Models," *Proceedings of the III Congress on Numerical Methods in Engineering*, edited by M. Doblaré, J. M. Correas, E. Alarćon, L. Gavete, and M. Pastor, SEMNI, Barcelona, 1996, pp. 875–885.

[9] "Metals Test Methods and Analytical Procedures," *Annual Book of ASTM Standards*, American Society for Testing and Materials, Philadelphia, 1988, Sec. 3.

[10] *Aluminium and Aluminium Alloys*, The Materials Information Society, ASM International, Chagrin Falls, OH, 1993, pp. 499–502.

[11] Celentano, D., "A Large Strain Thermoviscoplastic Formulation for Solidification of S.G. Cast Iron in a Green Sand Mould," *International Journal of Plasticity*, Vol. 17, 2001, pp. 1623–1658.

[12] Doyle, T., and Ericksen, J., "Nonlinear Elasticity," *Advances in Applied Mechanics*, Vol. 4, 1956, pp. 53–115.

[13] Coleman, B., and Gurtin, M., "Thermodynamics with Internal State Variables," *Journal of Chemical Physics*, Vol. 47, No. 2, 1967, pp. 597–613.

[14] Malvern, L., *Introduction to the Mechanics of a Continuous Medium*, Prentice–Hall, Upper Saddle River, NJ, 1969, Chap. 6.

[15] Lubliner, J., *Plasticity Theory*, Macmillan, New York, 1990, Chaps. 1, 3, and 8 (in Spanish).

[16] Celentano, D., Gunasegaram, D., and Nguyen, T., "A Thermomechanical Model for the Analysis of Light Alloy Solidification in a Composite Mould," *International Journal of Solids and Structures*, Vol. 36, 1999, pp. 2341–2378.

[17] Zienkiewicz, O., and Taylor, R., *The Finite Element Method*, 4th ed. Vols. 1 and 2, McGraw–Hill, London, 1989.

[18] Crisfield, M., *Non-Linear Finite Element Analysis of Solids and Structures*, Vols. 1 and 2, Wiley, Chichester, England, U.K., 1991.

[19] Dieter, G., *Mechanical Metallurgy—SI Metric Edition*, McGraw–Hill, London, 1988, Chap. 8.

S. Saigal
Associate Editor